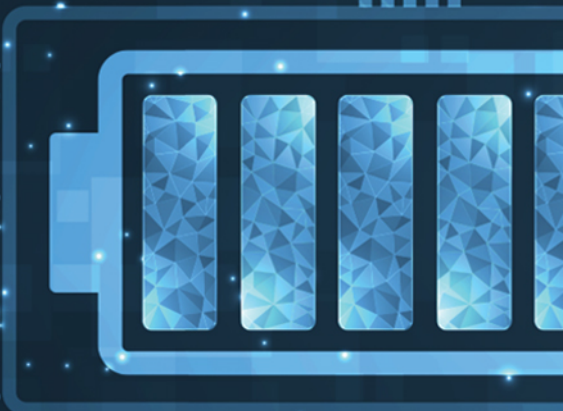


# ANALYTICAL SOLUTIONS TO DRIVE THE ENERGY REVOLUTION

Our comprehensive portfolio of analytical solutions for battery materials testing has the flexibility to support ongoing innovations and keep up with your laboratory's ever-changing requirements.

Carry out investigations to improve the performance, positivity, conductiveness and other properties of your battery parts such as cathode, anode, electrolyte, separators, membranes, and binders.

Providing the chemical and material analysis you need, we help you innovate in batteries for safety, performance, power, longevity, scale and weight.



Learn more at  
[www.perkinelmer.com/category/energy-storage](http://www.perkinelmer.com/category/energy-storage)

  
**PerkinElmer**<sup>®</sup>  
*For the Better*

# Model-Based Overpotential Deconvolution, Partial Impedance Spectroscopy, and Sensitivity Analysis of a Lithium-Ion Cell with Blend Cathode

Michael Quarti\* and Wolfgang G. Bessler

Lithium-ion battery cells are multiscale and multiphysics systems. Design and material parameters influence the macroscopically observable cell performance in a complex and nonlinear way. Herein, the development and application of three methodologies for model-based interpretation and visualization of these influences are presented: 1) deconvolution of overpotential contributions, including ohmic, concentration, and activation overpotentials of the various cell components; 2) partial electrochemical impedance spectroscopy, allowing a direct visualization of the origin of different impedance features; and 3) sensitivity analyses, allowing a systematic assessment of the influence of cell parameters on capacity, internal resistance, and impedance. The methods are applied to a previously developed and validated pseudo-3D model of a high-power lithium-ion pouch cell. The cell features a blend cathode. The two blend components show strong coupling, which can be observed and interpreted using the results of overpotential deconvolution, partial impedance spectroscopy, and sensitivity analysis. The presented methods are useful tools for model-supported lithium-ion cell research and development.

## 1. Introduction

The key characteristics of electrical energy storage devices such as lithium-ion batteries are energy, power, lifetime, safety, and cost. These characteristics are often represented in a spider-web type plot,<sup>[1–3]</sup> and the improvement of any single of these properties is, in practice, often detrimental to the others. The properties are closely related to the electrochemistry, the materials, and the design of the battery cells, leading to a classical optimization problem where a number of adjustable design parameters (such as electrode thickness or particle sizes) should be selected in order to achieve optimum macroscopic behavior

(such as internal resistance, affecting power capability, or cell capacity, affecting energy content).

Modeling and simulation are very useful tools in this regard: first because they allow the assessment of a large variety of virtual cell designs in short simulation times, and second because they enable the understanding of the underlying design-performance relationships. Therefore, simulations were used, for example, to improve lithium-ion cells<sup>[4,5]</sup> or to investigate the design of lithium-air cells.<sup>[6]</sup> To perform reliable computational design studies, the underlying models need to be predictive and validated. This requires physiochemical modeling approaches based on conservation equations on multiple scales, as widely used today for lithium-ion batteries.<sup>[7–12]</sup>

In the current study, we use a previously developed and validated model of a lithium-ion pouch cell<sup>[13]</sup> to develop and apply three

methods for cell performance analysis: 1) deconvolution of overpotential into individual contributions, 2) partial electrochemical impedance spectroscopy, and 3) sensitivity analysis. The overpotential  $\eta$  is defined<sup>[14,15]</sup> as the difference between operation voltage  $V$  and equilibrium voltage  $V^{\text{eq}}$

$$\eta = V - V^{\text{eq}} \quad (1)$$

The overpotential is (per this definition) negative for battery discharge (where  $V < V^{\text{eq}}$ ) and positive for battery charge (where  $V > V^{\text{eq}}$ ). It nonlinearly depends on state of charge (SOC), temperature  $T$ , and current  $I$ . The concept of the overpotential is useful because it is directly related to the internal resistance  $R_i$  of the cell according to Ohm's law


$$R_i = -\frac{dV}{dI} = -\frac{d\eta}{dI} \quad (2)$$

Overpotentials also lead to irreversible heat losses  $\dot{Q}$

$$\dot{Q} = -\eta \cdot I \quad (3)$$

which, in turn, is a measure for the electrical efficiency of the cell. Note that we define the current  $I$  positive for a discharge of the cell; therefore, the signs introduced to Equation (2) and (3) result in positive  $R_i$  and  $\dot{Q}$  for both discharge and charge.

M. Quarti, Prof. W. G. Bessler  
Institute of Energy Systems Technology (INES)  
Offenburg University of Applied Sciences  
Badstrasse 24, 77652 Offenburg, Germany  
E-mail: michael.quarti@hs-offenburg.de

 The ORCID identification number(s) for the author(s) of this article can be found under <https://doi.org/10.1002/ente.202001122>.

© 2021 The Authors. Energy Technology published by Wiley-VCH GmbH. This is an open access article under the terms of the Creative Commons Attribution License, which permits use, distribution and reproduction in any medium, provided the original work is properly cited.

DOI: 10.1002/ente.202001122

Overpotentials are also at the origin of the capacity-rate effect, that is, the apparent decrease in cell capacity with increasing current. As high temperatures and high (charging) overpotentials accelerate unwanted side reactions such as the formation of the solid electrolyte interface (SEI),<sup>[16,17]</sup> overpotentials are also indirectly related to cell lifetime. Therefore, overpotentials strongly influence many important macroscopic cell properties (energy, power, lifetime) and it is worthwhile quantifying, analyzing, and understanding their origin and properties. In the current study, we deconvolute the overall overpotential  $\eta$  into individual contributions  $\eta_k$  of electrochemistry of both electrodes, various transport processes, and ohmic losses. This enables a physicochemical interpretation of overpotential as function of, for example, current or temperature.

Electrochemical impedance spectroscopy (EIS) measures the frequency-dependent behavior of the alternating current (AC) resistance of the cell.<sup>[18]</sup> The complex frequency-domain impedance  $Z^*(\omega)$  is given by complex division of the Fourier transforms of  $V(t)$  and  $I(t)$  according to

$$Z^*(\omega) = -\frac{\mathcal{F}\{V(t)\}}{\mathcal{F}\{I(t)\}} \quad (4)$$

Using dynamic models, the impedance of lithium-ion batteries and other electrochemical cells can be simulated.<sup>[13,19–21]</sup> The simulations allow the assignment of physicochemical processes to the impedance features. In the current study, we introduce the concept of partial impedance spectroscopy. We define the partial impedance as

$$Z_{k^*}(\omega) = -\frac{\mathcal{F}\{\eta_k(t)\}}{\mathcal{F}\{I(t)\}} \quad (5)$$

This means that we use individual overpotential contributions  $\eta_k$  for simulating the individual impedance responses. This allows a direct visualization and interpretation of the magnitude and shape of the impedance of the underlying physicochemical processes.

Complex and nonlinear chemical systems such as lithium-ion battery cells are governed by many different parameters. A sensitivity analysis allows to quantify the influence of individual physicochemical parameters (e.g., rate constants, transport coefficients) on macroscopic observables (e.g., internal resistance). The method originates from the field of combustion, where it allows to quantify the influence of the kinetics of hundreds of chemical reactions on observables such as the flame speed or pollutant formation.<sup>[22–24]</sup> The method was later applied to heterogeneous catalytic reactions<sup>[25]</sup> and to solid oxide fuel cells.<sup>[21,26]</sup> In the current study, we show a systematic application to a lithium-ion battery cell.

This article is structured as follows. In Section 2, we present the physicochemical cell model and develop the framework for overpotential deconvolution. In Section 3, we introduce the simulation methodologies for partial impedance spectroscopy and sensitivity analyses. Results are presented and discussed in Section 4. Finally, the key findings are summarized in Section 5.

## 2. Model

### 2.1. Pseudo-3D Model

The study presented here is based on a physicochemical model previously developed and validated for a commercial 350 mAh high-power lithium-ion pouch cell with graphite anode and nickel cobalt aluminum oxide (NCA)/lithium cobalt oxide (LCO) blend cathode. A description of the development and parametrization of the model is available in Carelli et al.<sup>[13]</sup> The transport equations were derived by Kupper et al.<sup>[27]</sup> A summary of all model equations as well as symbol definitions are given in the Appendix.

In summary, the modeling framework is based on a 1D + 1D + 1D (pseudo-3D or P3D) multiscale modeling domain. A schematic of the modeling domain is also illustrated in the Appendix. The transport scales combine heat transport through the cell thickness (in this article referred to as macroscale or  $x$  scale), mass and charge transport inside the liquid electrolyte (mesoscale,  $y$  scale), and diffusive mass transport in the active material (AM) particles (microscale,  $z$  scale). Main assumptions of the transport model are the following: 1) heat transport on the macroscale is assumed conductive, and heat losses at the boundaries are modeled as combined convective and radiative. 2) On the mesoscale, the electrodes are described in a continuum setting, that is, microstructure is not resolved. Multispecies mass and charge transport in the electrolyte is described with combined diffusion and migration. 3) On the microscale, lithium transport in the AM is modeled by Fickian diffusion with stoichiometry-dependent diffusion coefficients. 4) The three scales are coupled through boundary conditions as well as chemistry and heat source terms. Electrochemistry is modeled in a consistent thermodynamic and kinetic setting as implemented in the open-source software Cantera.<sup>[28,29]</sup>

In Carelli et al.,<sup>[13]</sup> the model was validated against experimental data, in particular the voltage and temperature behavior during constant current constant voltage (CCCV) charge and discharge curves at three different temperatures (5, 20, 35 °C) and different C-rates (0.05, 1, 2, 5, 10 C), as well as electrochemical impedance spectra at three different temperatures (5, 20, 35 °C) and different SOC. The model showed good agreement over this complete experimental data set, with an exception of the low-frequency (< 0.1 Hz) impedance behavior which is underpredicted by the model. In the current study, we show available experimental data of cell voltage and total overpotential from Carelli et al.<sup>[13]</sup> The validation of individual overpotential contributions and partial electrochemical impedance spectra would require elaborate analysis of experimental impedance spectra, and the validation of the sensitivity analysis would require systematic variational experimental studies, both of which are out of scope of the present contribution.

### 2.2. Quantification of Overpotential Contributions

The total overpotential of an electrochemical cell, defined by Equation (1), is caused by slow transport processes and slow reactions within the different components of cell. In the following, we show how the contribution of each individual transport or reaction process can be quantified using the physicochemical

model described in the previous section. In particular, we distinguish between the following overpotential contributions: on the macroscale, 1) the ohmic overpotential due to electron transport in the current collection system,  $\eta_{cc}$ ; on the mesoscale, 2) the ohmic overpotential due to ion transport in the electrolyte,  $\eta_{ohm,elyte}$ , and 3) the concentration overpotential caused by lithium ion concentration changes,  $\eta_{conc,elyte}$ ; and on the microscale, 4) the activation overpotentials of the charge-transfer reactions,  $\eta_{act,AM}$  (one contribution for each individual AM), and 5) the concentration overpotentials due to solid-state lithium transport in the intercalation compounds,  $\eta_{conc,AM}$  (again one contribution for each individual AM). As the investigated cell has a total of three AMs (one at the negative electrode and two at the positive blend electrode), there is a total of nine individual contributions to the total overpotential to be considered.

### 2.2.1. Ohmic Overpotential of the Current Collection System

The resistance of the current collectors is described in the model as simple Ohmic process given by a single model parameter, the current collection resistance  $R_{cc}$ . This resistance leads to an overpotential with a strict ohmic behavior given by

$$\eta_{cc} = -i \cdot R_{cc} \quad (6)$$

where  $i$  is the current density of the cell (current with respect to the active electrode area). The minus sign arises from the combination of our (chosen) convention that positive  $i$  is assigned to cell discharge, and the (common) convention that overpotentials are negative for cell discharge, as defined in Equation (1).

### 2.2.2. Ohmic Overpotential of the Electrolyte

During charging and discharging, ion transport in the electrolyte causes a gradient in the ionic potential along the mesoscale which is influenced by the transport parameters of the electrolyte and the pore-space properties. This situation is shown in **Figure 1**. Panel (a) shows the ionic potential as function of mesoscale coordinate at the end of a 5 C CC discharge. The potential monotonically increases along the mesoscale distance. The electrode-averaged values as well as the cell-averaged value are also shown in this panel. Note that the value of the latter depends on the SOC of the cell.

The ionic potential and, therefore, overpotentials depend on the  $y$  position within the cell (note that  $y$  defines the mesoscale, cf., Figure A1 in the Appendix). Figure 1b schematically illustrates the situation for a cathode half-cell (corresponding to the left part of panel (a)) that is assumed to be governed only by ohmic overpotentials in the electrolyte and activation overpotentials of the electrochemical reaction. Scheme *i* represents equilibrium (no current flowing). Scheme *ii* represents an ideal, infinitely conductive electrolyte. Here, the total overpotential  $\eta = \eta_{act} = \Delta\phi - \Delta\phi^{eq}$  has only one contribution, that is, the activation overpotential  $\eta_{act}$ , which is therefore independent of the  $y$  position. Scheme *iii* represents a real electrolyte with finite conductivity for the same total overpotential  $\eta$  as in Scheme *ii*. Here, the potential has a gradient. Although the total overpotential  $\eta$  is spatially constant, it is now composed of two contributions, the activation overpotential  $\eta_{act}(y)$  and the electrolyte ohmic

overpotential  $\eta_{ohm}(y)$ , both of which are spatially varying. Scheme *iv* shows a case for an electrolyte with low conductivity (or for a very thick electrode). Here,  $\eta_{ohm}(y)$  dominates over a large part of the electrode.

In all these cases, we can deconvolute the macroscopic  $\eta$  into its contributions by using simple arithmetic averaging

$$\eta = \eta_{act}(y) + \eta_{ohm}(y) = \langle \eta_{act}(y) \rangle_{ca} + \langle \eta_{ohm}(y) \rangle_{ca} \quad (7)$$

Here and in the following, we use angle brackets to denote a spatial average, and the spatial domain the average is taken over is denoted as subscript (ca = cathode, se = separator, an = anode). Using only the electrolyte potential, the average ohmic overpotential can be expressed as

$$\langle \eta_{ohm}(y) \rangle_{ca} = \langle \phi_{elyte} \rangle_{ca} - \phi_{elyte,se} \quad (8)$$

where  $\phi_{elyte,se}$  is the electrolyte potential at the cathode/separator interface (indicated as green dot in Figure 1b). It should be noted that, during averaging, no weighting by the local current density is required. In scheme *iv*, for example, the largest part of the electrode is electrochemically inactive ( $\Delta\phi = \Delta\phi^{eq}$ , therefore no local current flowing). This is because the ohmic overpotential takes effect over the whole electrode thickness. Therefore, it should not be weighted with the local current density during averaging. The same argument applies to other overpotential contributions, for example, the concentration overpotential (cf., further later).

In the full cell (Figure 1a), there are electrolyte ohmic losses in both electrodes and in the separator. Using the same approach for averaging, we combine them to a total ohmic overpotential as

$$\eta_{ohm,elyte} = \langle \phi_{elyte}(y) \rangle_{ca} - \langle \phi_{elyte}(y) \rangle_{an} \quad (9)$$

This is the final expression for the  $\eta_{ohm,elyte}$  used in the further analyses.

### 2.2.3. Concentration Overpotential due to Electrolyte Transport

Charging and discharging also leads to a concentration gradient of lithium ions in the electrolyte. **Figure 2a** shows the lithium ion concentration as function of mesoscale coordinate at the end of a 5 C CC discharge. The concentration variation affects the local reaction thermodynamics, which can be quantified as a local overpotential given by

$$\eta_{conc,elyte,local}(y) = -\frac{R \cdot T}{F} \cdot \ln \frac{c_{Li^+}(y)}{\langle c_{Li^+}(y) \rangle_{ca,se,an}} \quad (10)$$

where  $R$  is the ideal gas constant,  $T$  is the temperature,  $F$  is Faraday's constant, and  $c$  is the molar concentration. Using the nomenclature for averaging as defined in the previous section, the term  $\langle c_{Li^+}(y) \rangle_{an,se,ca}$  refers to the average lithium-ion concentration over cathode, separator, and anode. As lithium-ion transport is confined to these domains, this value corresponds to equilibrium and therefore the reference for the overpotential definition. The local concentration overpotential is plotted as function of position in Figure 2b. It is negative in the cathode and positive in the anode.

Although the local values affect the local reaction properties, further spatial averaging is required to derive the global



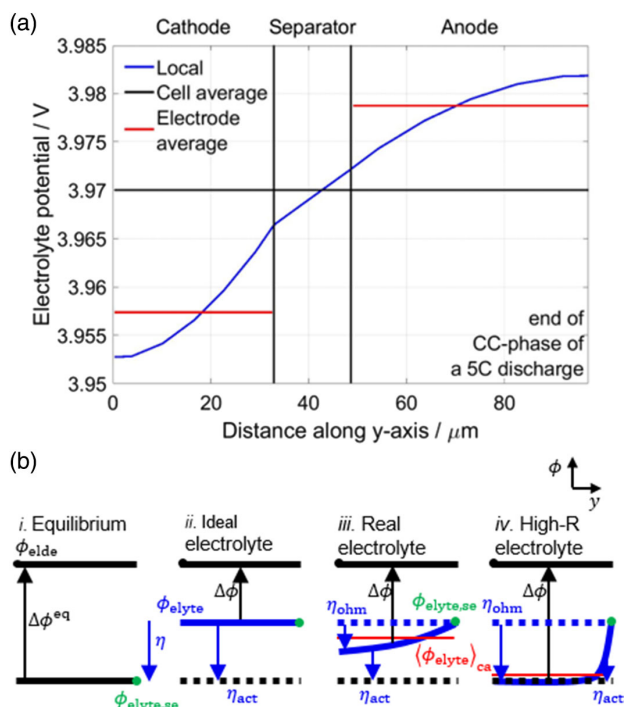


**Figure 1.** a) Ionic potential in the electrolyte as function of distance along the mesoscale. These data were taken at the end of 5 C constant-current discharge at 20 °C ambient temperature. b) Schematic representation of potentials and overpotentials in the cathode for different scenarios. The spatial scale shown in the schemes corresponds to the left part (cathode) of panel (a).

overpotential. We first average over the respective electrodes,  $\langle \eta_{\text{conc,elyte,local}}(y) \rangle_{\text{an}}$  and  $\langle \eta_{\text{conc,elyte,local}}(y) \rangle_{\text{ca}}$ . These electrode-averaged values are also shown in Figure 2b, together with the cell average which is zero per definition of Equation (10). Finally, the macroscopically observable concentration overpotential results from a combination of the overpotential of both electrodes according to

$$\eta_{\text{conc,elyte}} = \langle \eta_{\text{conc,elyte,local}}(y) \rangle_{\text{an}} - \langle \eta_{\text{conc,elyte,local}}(y) \rangle_{\text{ca}} \quad (11)$$

This expression is consistent with the sign convention that overpotential is negative upon discharge.

#### 2.2.4. Activation Overpotential of an Individual Charge-Transfer Reaction

The charge-transfer reaction at the AMs particle surface leads to an activation overpotential, which is generally given as

$$\eta_{\text{act,local}}(y) = \Delta\phi(y) - \Delta\phi^{\text{eq}}(y, z = 0) \quad (12)$$

where  $\Delta\phi = \phi_{\text{elde}} - \phi_{\text{elyt}}$  is the local potential difference between electrode and electrolyte<sup>[30]</sup> and  $\Delta\phi^{\text{eq}}$  is the equilibrium potential of the charge-transfer reaction. The latter is a local property, that is, it depends on the local (on the  $y$  scale) ion concentration in the electrolyte and the particle surface ( $z = 0$ ) lithium concentration. We calculate the macroscopic activation overpotential as electrode average according to

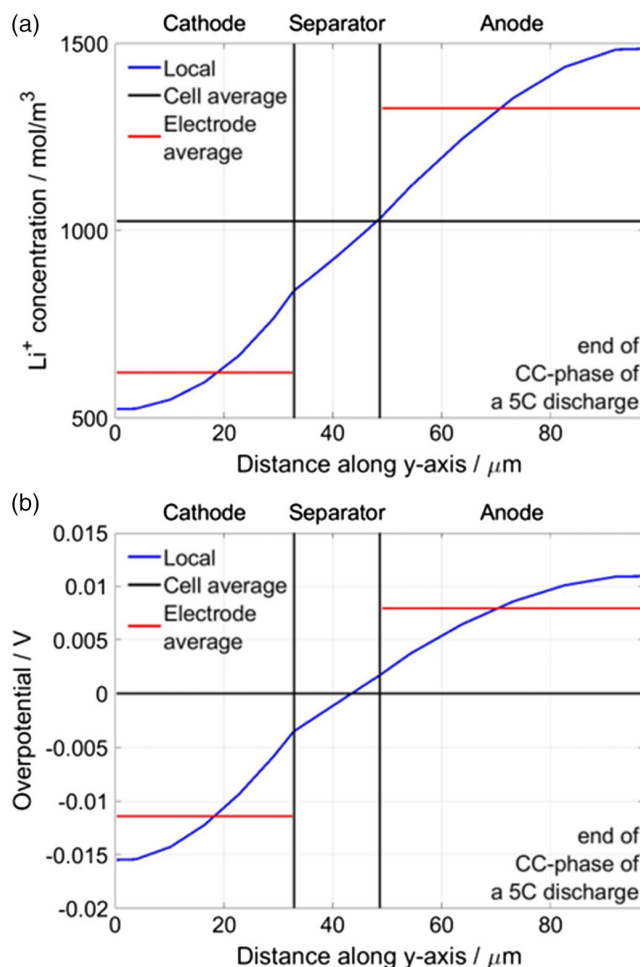


**Figure 2.** Behavior on the mesoscale ( $y$  scale): a) lithium-ion concentration gradient, b) resulting local and averaged concentration overpotentials. These data were taken at the end of 5 C constant-current discharge at 20 °C ambient temperature.

$$\eta_{\text{act,ca,AM}_i} = \langle \eta_{\text{act,local,AM}_i}(y) \rangle_{\text{an}} \quad (13)$$

$$\eta_{\text{act,an,AM}_i} = -\langle \eta_{\text{act,local,AM}_i}(y) \rangle_{\text{ca}} \quad (14)$$

for individual AMs  $i$  at anode and cathode, respectively.

#### 2.2.5. Concentration Overpotential of the AMs

The finite solid-state diffusion rate of lithium within the AM causes a lithium concentration profile along the radius of the particle, giving rise to a concentration overpotential. It is a local value on the mesoscale, given by the difference between the surface equilibrium potential of the nonequilibrated particle and the equilibrium potential of a transport-equilibrated particle according to

$$\eta_{\text{conc,local}}(y) = \Delta\phi^{\text{eq}}(X_{\text{Li}}(y, z = 0)) - \Delta\phi^{\text{eq}}(X_{\text{Li}}^{\text{eq}}(y)) \quad (15)$$

The equilibrium half-cell potentials  $\Delta\phi^{\text{eq}}$  are obtained from Cantera. Again, we take electrode averages

$$\eta_{\text{conc,an,AM}_i} = \langle \eta_{\text{conc,local,AM}_i}(y) \rangle_{\text{an}} \quad (16)$$

$$\eta_{\text{conc,ca,AM}_i} = -\langle \eta_{\text{conc,local,AM}_i}(y) \rangle_{\text{ca}} \quad (17)$$

For an electrode consisting of a single AM (graphite anode in the present case), the equilibrium lithium stoichiometry is simply the particle average (intraparticle equilibration)

$$X_{\text{Li}}^{\text{eq}} = \langle X_{\text{Li}}(z) \rangle_{\text{particle}} \quad (18)$$

For averaging we consider the spherical particle shape (outer portions of the particle represent a larger fraction of the total volume). **Figure 3** compares lithium stoichiometry profiles along the microscale at the end of a 5 C discharge and after equilibration. A representative graphite particle is shown in panel (a). Note that, for the particle average, the spherical geometry results in higher weights of the particle outer volumes.

For an electrode with more than one AM (LCO/NCA cathode in the present case), the situation is more complex. As the particles are in electronic and (via the electrolyte) in ionic contact, they will exchange lithium until equilibrium is reached (interparticle equilibration). This is the case when all materials are at the same potential, for two AMs given as

$$\Delta \phi_{\text{AM}_1}^{\text{eq}} \left( X_{\text{Li,AM}_1}^{\text{eq}} \right) = \Delta \phi_{\text{AM}_2}^{\text{eq}} \left( X_{\text{Li,AM}_2}^{\text{eq}} \right) \quad (19)$$

The equilibrium stoichiometries  $X_{\text{Li,AM}_1}^{\text{eq}}$  and  $X_{\text{Li,AM}_2}^{\text{eq}}$  generally differ from each other. The concentration overpotential  $\eta_{\text{conc,local}}(y)$ , as defined in Equation (16), includes contributions from interparticle transport—even if the intraparticle transport is fast (e.g., for very small particles),  $\eta_{\text{conc,local}}(y) \neq 0$ . This is illustrated in panels (b,c) of Figure 3 for LCO and NCA, respectively. Here, interparticle equilibration leads to an overall increase in LCO stoichiometry and decrease in NCA stoichiometry, compared with the dynamic profile. In all panels of Figure 3, black arrows indicate the difference of the particle surface stoichiometries between dynamic case and equilibrium. It is this stoichiometry difference that gives rise to the concentration overpotential. In case of the LCO/NCA system, the concentration overpotentials have opposite signs for the two AMs. The equilibrium concentration is not the intraparticle average, but the weighted (by the individual potential curves) interparticle average.

It should be noted that, because in the blend electrode both AMs are subjected to the same local half-cell potential, their total overpotential (consisting of activation and concentration parts) must be the same. This is mathematically described as

$$\eta_{\text{act+conc,ca}} = \eta_{\text{act,ca,LCO}} + \eta_{\text{conc,ca,LCO}} = \eta_{\text{act,ca,NCA}} + \eta_{\text{conc,ca,NCA}} \quad (20)$$

For this reason, it is not possible to express the total cathode overpotential as sum of the four individual contributions—only as the sum  $\eta_{\text{act}}$  and  $\eta_{\text{conc}}$  for an individual AM, which has the same value for both AM. Therefore, in Section 4, only the total cathode overpotential is given. **Figure 4** shows the separation of the four cathode overpotentials during a 5 C CCCV charge/discharge cycle as function of charge throughput, the upper panel for LCO and the lower panel for NCA. The solid black lines represent the total overpotential  $\eta_{\text{act+conc,ca}}$ . They are identical for both materials. The dashed lines represent the individual

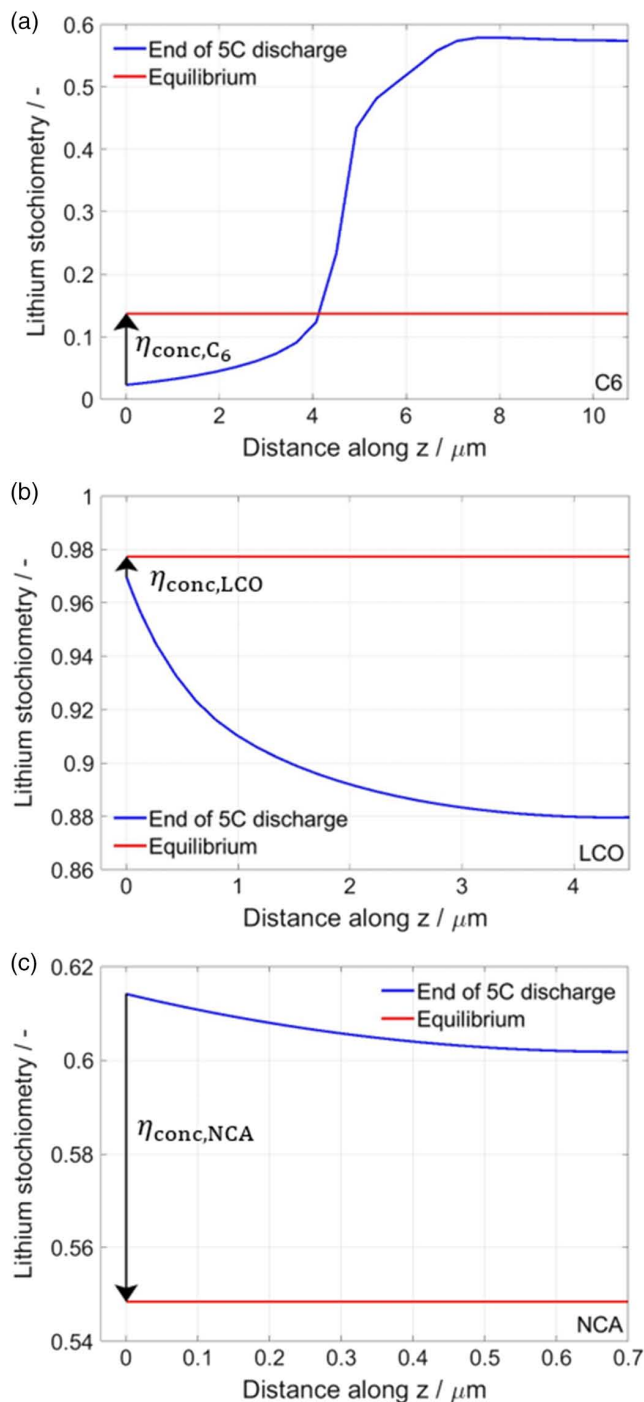


**Figure 3.** Lithium stoichiometry along the AM radius ( $z$  dimension) at the end of the CC phase of a 5 C CCCV discharge, and after equilibration. a) Graphite, b) LCO, and c) NCA. The arrows indicate the difference between dynamic and equilibrated particle surface stoichiometries, being the origin of the (intraparticle and interparticle) concentration overpotential.

activation overpotentials. The difference between total and activation overpotential, which is the area between the two lines, is the concentration overpotential. For better illustration, we have

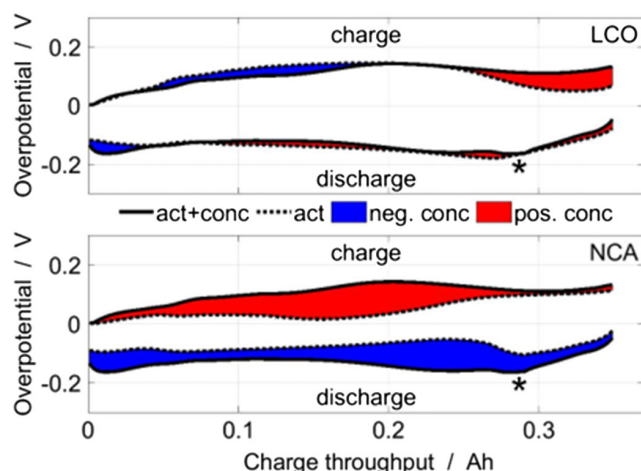


**Figure 4.** Concentration and activation overpotential contributions of the two AMs in the blend cathode during a CCCV cycle with 5 C at 20 °C. The asterisks mark the point where the profiles shown in Figure 3 were taken.

colored this area in red and blue depending on the sign of the concentration overpotential. For NCA, the overpotentials remain “sorted” throughout the cycle (at discharge: negative activation, concentration, and total overpotentials). For LCO, however, there are points where the concentration overpotential changes sign, leading to a crossing of activation and total overpotentials. The asterisks shown in Figure 4 mark the moment during discharge where the profiles shown in Figure 3 were taken. At this point, for LCO, concentration and activation overpotentials have opposite signs (Figure 4), and during equilibration the lithium stoichiometry continues increasing (Figure 3). These observations illustrate the complex behavior of blend electrodes.

#### 2.2.6. Overall Contribution

The total overpotential of the cell is given as sum of the individual contributions derived earlier

$$\eta = \eta_{cc} + \eta_{conc,elyte} + \eta_{ohm,elyte} + \eta_{act,an} + \eta_{conc,an} + \eta_{act+conc,ca} \quad (21)$$

As discussed earlier, the individual contributions of the blend electrode overpotentials can be separated out only for an individual AM.

The total overpotential calculated from Equation (22) as function of charge throughput can be compared with a global overpotential obtained from comparison to a quasi-equilibrium curve

$$\eta_{global}(Q) = V(Q) - V^{C/100}(Q) \quad (22)$$

where  $Q$  is the charge throughput,  $V$  is the simulated cell voltage during discharge (e.g., with a 5 C rate), and  $V^{C/100}$  is the simulated cell voltage during very slow discharge with  $C/100$  rate (quasi-equilibrium). The simulations show a small deviation between  $\eta$  and  $\eta_{global}$ ; for a 5 C cycle at 20 °C, the maximum deviation is 1.6%. These deviations vanish when the model is reduced to a single-particle model (no gradients within the electrode in  $y$  direction). We therefore assign the deviations to the

averaging over the electrode dimension, which is reasonable given the nonlinear dependence of overpotentials on local states (concentrations, potentials). In the following overpotential analysis (Section 4.1), the individual overpotentials were proportionally corrected for the deviation in a postprocessing step by applying a correction factor

$$f_{\eta} = \frac{V_{chg} - V_{dis} - (\eta_{cc}^{chg} - \eta_{cc}^{dis})}{\sum_k \eta_k^{chg} - \eta_k^{dis}} \quad (23)$$

where  $k = \{\text{conc}_{elyt}, \text{ohm}_{elyt}, \text{conc}_{an}, \text{act}_{an}, \text{act} + \text{conc}_{ca}\}$ . Only  $\eta_{cc}$  is excluded from this correction because it does not involve averaging (cf., Equation (6)).

### 3. Simulation

#### 3.1. Charge/Discharge Protocol and Overpotential Calculation

The charge/discharge behavior of cell is simulated by a commonly used CCCV protocols. In particular, we simulate charge (CC to 4.2 V, CV until current drops below  $C/50$ ), rest (30 min), and discharge (CC to 3.0 V, CV until current drops below  $C/50$ ). Different CC-phase currents were applied and compared in the following studies. CV phases are used both during charge and during discharge, allowing for clear “full” and “empty” battery states, respectively.<sup>[13,31]</sup> Throughout this article, we define the C-rate as

$$\text{C-rate} = \frac{I \cdot 1h}{C_N} \quad (24)$$

with  $C_N = 0.35$  Ah for the investigated cell (cf., Section 2.1).

The overpotentials were calculated by inserting the simulated state variables (current, potentials, concentrations) into the equations given in Section 2.2. For the concentration overpotentials in the cathode,  $\eta_{conc,ca,LCO}$  and  $\eta_{conc,ca,NCA}$ , a simple iterative algorithm was used to equilibrate the potential of the AMs.

#### 3.2. Partial EIS Simulation

For simulating the partial EIS presented within this study, a voltage step method<sup>[32]</sup> is used. Starting from a rested cell at  $t = 0$ , we apply a fast linear voltage step with a step length of  $\tau = 10^{-7}$  s and step height  $\Delta V = -0.005$  V described by

$$V(t) = V_0 + \frac{t}{\tau} \Delta V \quad t < \tau \quad (25)$$

$$V(t) = V_0 + \Delta V \quad t > \tau \quad (26)$$

The step excitation results in a dynamic current response  $I(t)$ . The simulated current peaks at values around 290 mA, corresponding to a 0.83 C rate. Total simulation time was  $10^6$  s. The complex frequency-domain impedance  $Z^*(\omega)$  is given by the complex division of the Fourier transforms of  $V(t)$  and  $I(t)$  according to Equation (4).

In analogy, we apply Equation (4) to the different overpotential contributions quantified in Section 2.2

$$Z_k^*(\omega) = -\frac{\mathcal{F}\{\eta_k(t)\}}{\mathcal{F}\{I(t)\}} \quad (27)$$

where  $k = \{\text{cc}, \text{conc}_{\text{elyt}}, \text{ohm}_{\text{elyt}}, \text{act}_{\text{an}}, \text{act}_{\text{LCO}}, \text{act}_{\text{NCA}}, \text{conc}_{\text{an}}, \text{conc}_{\text{LCO}}, \text{conc}_{\text{NCA}}\}$ . We refer to the resulting  $Z_k^*$  as partial impedance, and its frequency dependency as partial impedance spectrum. Just as the sum of all overpotential contributions gives rise to the total overpotential, the sum of all partial impedance responses results in the total impedance

$$Z^*(\omega) = Z_{\text{cc}}^*(\omega) + Z_{\text{conc,elyt}}^*(\omega) + Z_{\text{ohm,elyt}}^*(\omega) + Z_{\text{act,an}}^*(\omega) + Z_{\text{conc,an}}^*(\omega) + Z_{\text{act+conc,ca}}^*(\omega) \quad (28)$$

The simulations are conducted as follows. First, the virtual cell is driven to a given SOC. To this goal, starting with a fully charged cell, a discharge (1 C CC to 3.0 V, CV with C/20 cutoff), rest (1 h), charge (1 C CC to 4.2 V, CV with C/20 cutoff), rest (1 h), discharge (C/10, CC) to given SOC and rest (12 h) is simulated. Afterward we simulate the step excitation as described earlier.

### 3.3. Sensitivity Analysis

To identify the most significant parameters of the cell, a sensitivity analysis was performed.<sup>[26]</sup> We chose three target observables  $O_j$  for the analysis: the cell capacity  $C$ , the internal resistance  $R_i$  at 50% SOC, and the absolute value of the impedance at 1 kHz  $|Z(1 \text{ kHz})|$ . These represent the most important macroscopic cell characteristics, also typically given in data sheets. Furthermore, we performed sensitivity analyses using the overpotential contributions  $\eta_k$  as target observables.

The sensitivity of a total of 20 model parameters  $P_i$  on these observables was calculated, including macroscale (cell thickness  $d_{\text{cell}}$ , heat conductivity  $\lambda$ , heat capacity  $c_p$ , current collector resistance  $R_{\text{cc}}$ ), mesoscale (anode, cathode, and separator thicknesses  $d_{\text{an}}, d_{\text{ca}}, d_{\text{se}}$ , ion diffusion coefficients  $D_{\text{Li}^+}, D_{\text{PF}_6^-}$ ), microscale (particle radii  $r_{\text{C}_6}, r_{\text{LCO}}, r_{\text{NCA}}$ , solid-state diffusion coefficients  $D_{\text{Li,C}_6}, D_{\text{Li,LCO}}, D_{\text{Li,NCA}}$ ), and electrochemistry (exchange current density factor  $i_{\text{C}_6}^0, i_{\text{LCO}}^0, i_{\text{NCA}}^0$ , double-layer capacitances  $C_{\text{DL,an}}^V, C_{\text{DL,ca}}^V$ ). We refer the reader to the Appendix for a full definition of symbols and model equations.

Each model parameter  $P_i$  was individually changed by  $\pm 5\%$  from its original value  $P_i^0$  to  $P_i^+ = 1.05P_i^0$  and  $P_i^- = 0.95P_i^0$ . Then simulations were conducted and the observables  $O_j$  were quantified. Dividing the change in the observable  $\partial O_j^+ = (O_j^+ - O_j^0)/O_j^0$  and  $\partial O_j^- = (O_j^- - O_j^0)/O_j^0$  by the change in the parameter  $\partial P_i^+ = (P_i^+ - P_i^0)/P_i^0 = 0.05$  and  $\partial P_i^- = (P_i^- - P_i^0)/P_i^0 = -0.05$  results in the relative sensitivity

$$f_{ji} = \frac{1}{2} \left( \frac{\partial O_j^+}{\partial P_i^+} + \frac{\partial O_j^-}{\partial P_i^-} \right) \quad (29)$$

A sensitivity of  $f = 1$  means that the observable is directly proportional to the parameter. A sensitivity of  $f = -1$  means that the observable is inversely proportional to the parameter. Sensitivities close to zero mean that the parameter does not affect the observable. Sensitivities  $|f| > 1$  mean that the parameter strongly and nonlinearly affects the observable. The magnitude of parameter variation ( $\pm 5\%$ ) was chosen sufficiently large to be above the threshold of numerical noise (which was observed to

be important for parameters with low sensitivity), but sufficiently small to stay within linear response. All sensitivities therefore need to be interpreted with respect to the base cell parameters, while a significant change in the base parameters is likely to result in different sensitivities.

For each individual parameter set, the aforementioned observables were obtained as follows. For the capacity and the overpotentials, the protocol from Section 3.1 was used with 5 C rate. The capacity was determined at the end of the CCCV discharge and for the overpotentials the mean value between 40% and 60% SOC was used. The internal resistance was obtained by discharging the cell to an SOC of 50% using the protocol mentioned in Section 3.2.

A following 1 C step at  $t_0$  results in the internal resistance

$$R_i = -\frac{V_{t_0+3s} - V_{t_0}}{I_{t_0+3s} - I_{t_0}} \quad (30)$$

For the impedance at 1 kHz the protocol from Section 3.2 was used. The SOC values given here are taken with respect to the base model.

## 4. Results and Discussion

### 4.1. Overpotential Analysis

Simulated discharge and charge curves at 5 C rate and  $20^\circ\text{C}$  are shown in Figure 5, along with experimental data taken from Carelli et al.<sup>[13]</sup> Both charge and discharge were conducted with CCCV protocols to reach defined “full” and “empty” cell states after charge and discharge, respectively. The figure shows the overpotential contributions, quantified as described in Section 2.2, as colored areas. Thus, at each given charge throughput, the overpotential contributions sum up and add to the equilibrium voltage to yield the observed discharge ( $\eta < 0$ ) and charge ( $\eta > 0$ ) curves. The curves show how the different contributions depend individually on charge throughput. There is no single contribution dominating the overall behavior; however, ohmic overpotentials of the current collection system and electrolyte as well as concentration overpotential in the electrolyte

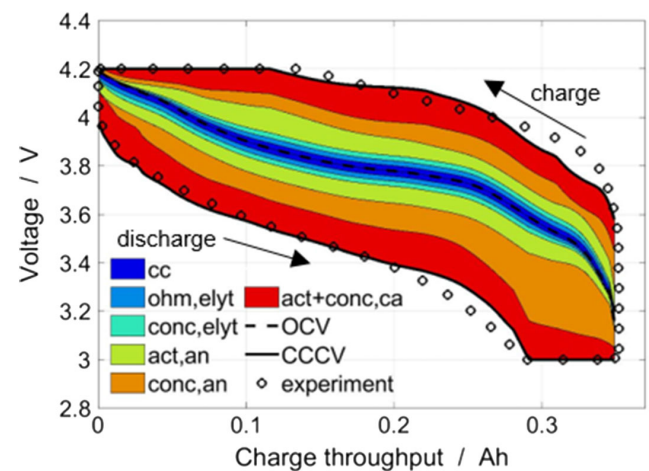


**Figure 5.** Discharge and charge curves during a CCCV cycle at 5 C,  $20^\circ\text{C}$  with deconvoluted overpotential contributions.



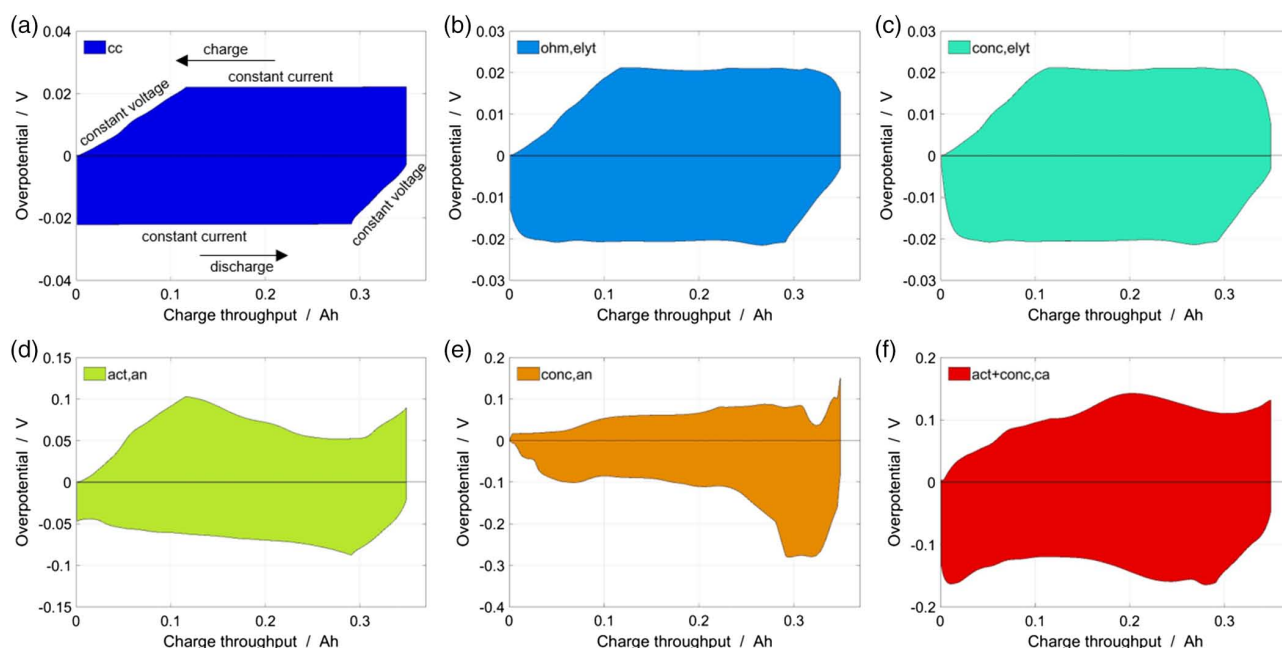


**Figure 6.** Separated overpotential contributions during a CCCV cycle at 5 C and 20 °C, showing the same data as in Figure 5 in a different representation.

are rather small. The drop of the discharge curve toward its cutoff voltage (charge throughputs of 0.25...0.3 Ah) is dominated by the anode concentration overpotential.

To better visualize the overpotential contributions, they are plotted individually in **Figure 6**, using data of the same simulation run as shown in Figure 5. The ohmic overpotential of the current collection system ( $\eta_{cc}$ , panel (a)) shows the expected (cf., Equation (6)) purely ohmic behavior. The value is constant during the CC phase, leading to plateaus in the plot, and opposite for discharge ( $\eta_{cc} < 0$ ) and charge ( $\eta_{cc} > 0$ ). The panel also well illustrates the CV phases toward end of discharge and end of charge, where decreasing current leads to proportionally decreasing overpotential. The absolute value is small, in the order of 20 mV. The ohmic overpotential of the electrolyte ( $\eta_{ohm,elyt}$ ) is shown in panel (b). It shows a similar shape and magnitude as  $\eta_{cc}$ , but the curve appears smoothed and slightly undulating—an effect of the dynamics of lithium ion diffusion and migration. A similar behavior is observed for the concentration overpotential of the electrolyte ( $\eta_{conc,elyt}$ ), shown in panel (c), having the same cause (ion transport) but different effect (equilibrium reaction potential).

The AMs show overpotentials that are an order of magnitude higher. For the graphite anode, we are able to separately assess activation and concentration contributions. The activation overpotential ( $\eta_{act,an}$ , panel (d)) shows a nonlinear and asymmetric (with respect to discharge and charge) behavior. This results from a combination of concentration-dependent exchange current density (cf., Appendix)

$$i^0 \sim c_{Li^+}^{0.5}[elyte] \cdot c_{Li}^{0.5}[C_6] \cdot c_V^{0.5}[C_6] \quad (31)$$

which is affected by both the solid-state lithium concentration and the electrolyte-phase lithium-ion concentration; and time-dependent equilibrium potential, which is a function of lithium

concentration on the AM particle surface and is therefore related to the intraparticle lithium diffusion. The concentration overpotential ( $\eta_{conc,an}$ , panel (e)) shows the largest individual contribution, with values peaking at  $-280$  mV during discharge and  $+150$  mV during charge. It shows a strong dependence on the SOC, which is due to the assumed stoichiometry-dependent diffusion coefficient (cf., solid-state concentration profiles given in Carelli et al.<sup>[13]</sup>). In particular, the negative peak at a charge throughput of around 0.3 Ah results from a hindering of the diffusion due to the minimum of the diffusion coefficient as function of stoichiometry.

For the LCO/NCA blend cathode, activation and concentration overpotentials cannot be deconvoluted (cf., Section 2.2.5) and are plotted as sum ( $\eta_{act+conc,ca}$ , panel (f)). The behavior is nonlinear, but less asymmetric compared with the anode. Values peak at  $-160$  mV during discharge and  $+140$  mV during charge.

We can use the model to study the dependence of overpotential magnitude and distribution on operation parameters, particularly C-rate and temperature. To this goal, CCCV discharge/charge cycles were conducted and the overpotentials were quantified at fixed states of charge, 80% for the discharge branch and 20% for the charge branch. These states were selected because they are well within the CC phase for most conditions. Results of this study are shown in **Figure 7**. C-rate variations at different temperatures are shown in panels (a–c), while temperature variations at different C-rates are shown in panels (d–f). The figure includes experimental data for the total overpotential for conditions measured by Carelli et al.<sup>[13]</sup> The simulations show, in agreement with the experiments, that overpotentials generally increase with increasing C-rate, and decrease with increasing temperature. The importance of the different contributions, however, changes. At 20 °C and low C-rates, the cathode ( $\eta_{act+conc,ca}$ ) dominates. At higher C-rates, the anode ( $\eta_{conc,an}$ ) dominates. At increasing temperature, the ohmic contributions ( $\eta_{cc}$  and  $\eta_{ohm,elyt}$ )

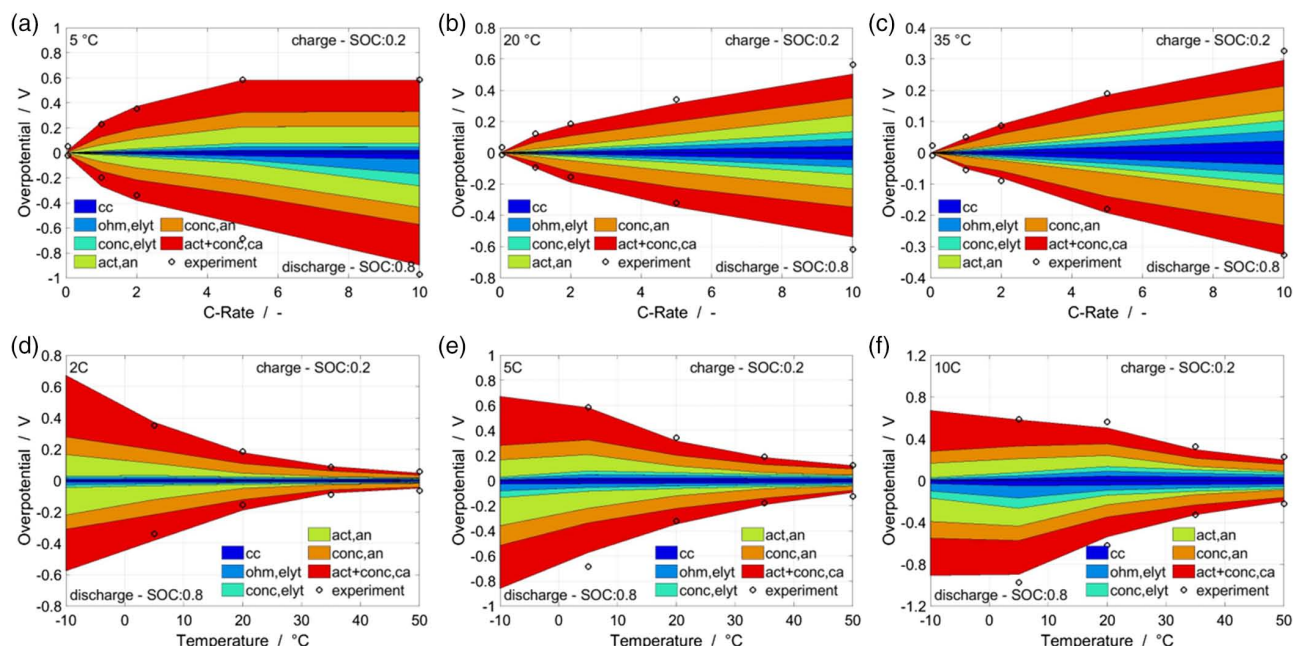


**Figure 7.** Dependence of the overpotential contributions on C-rate a–c) at fixed temperatures (5, 20, 35 °C) and d–f) on temperature with fixed C-rate (2, 5, 10 C).

become increasingly important. Also, the asymmetry between discharge and charge, as already discussed earlier, is quite obvious in these figures, caused mainly by the anode concentration overpotential, which is also the dominating contribution under most, yet not all, conditions. Toward low temperatures and high C-rates, the total overpotentials appear to saturate. This is because the system is already at the CV phase under these conditions.

Overall, the presented results show that different physico-chemical processes inside the cell contribute quite differently to the overall overpotential and furthermore nonlinearly depend on SOC, temperature, and current.

## 4.2. Partial EIS

In the previous section, we have investigated the time-domain behavior of individual overpotential contributions. Next, we study the frequency-domain behavior. To this goal we introduce the concept of partial electrochemical impedance spectroscopy, as defined and discussed in Section 3.2. Bode plots of the simulated partial impedance of the different processes  $Z_k$  are shown in Figure 8. The results show clearly how the different contributions are separated in the time domain. Panel (a) shows the real parts as function of logarithmic frequency. The largest contribution is that of the cathode ( $\eta_{\text{act+conc,ca}}$ ). This is consistent with the results of the time-domain analysis at low currents (see, e.g., Figure 7b; note the impedance simulation results in currents in the order of 0.83 C rate, which is in the lower part of the current range shown in Figure 7b). The sum of the individual contributions is shown as dashed line, corresponding to the total cell impedance.

The representation of the imaginary parts (Figure 8b) allows to visually separating the different contributions in a clearer way. At low frequencies ( $< 0.1$  Hz), the spectra are dominated by the

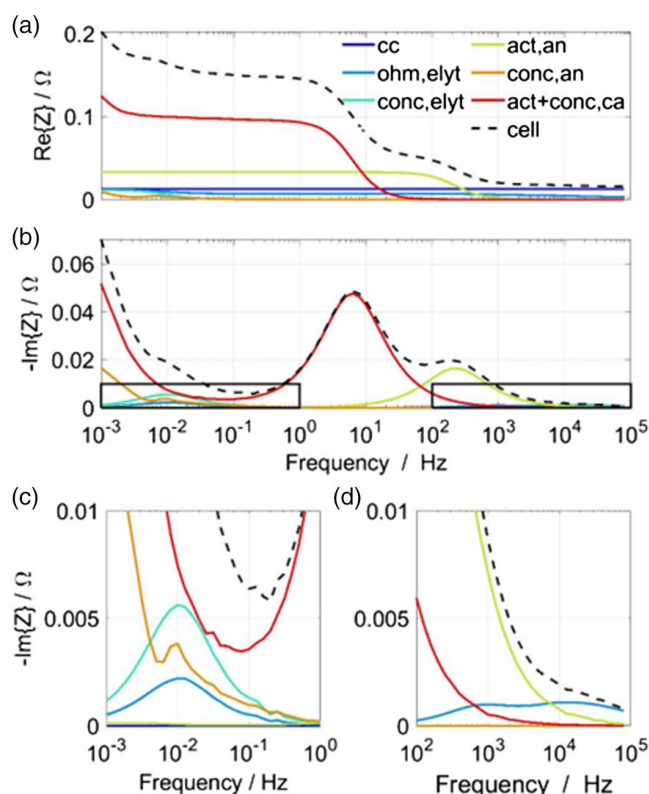


**Figure 8.** Partial electrochemical impedance spectra  $Z_k$  in Bode representation, simulated at 50% SOC and 20 °C. The dashed line is the sum of all contributions.

concentration impedances in cathode, anode, and electrolyte. At intermediate frequencies (1–10 Hz), the cathode activation impedance is important. At high frequencies (100–1000 Hz), the anode activation impedance dominates. These findings are consistent with common interpretations of electrochemical impedance spectra of lithium-ion battery cells.<sup>[33–35]</sup> Detail views of the negative imaginary part are shown in panels (d,e). Here, it is interesting to note that the electrolyte shows dynamic responses, both for the ohmic and the concentration impedances. It should be noted that the partial impedance simulation presented here allows a fast and straightforward way of assigning impedance features to physicochemical processes, without requiring equivalent circuit fits or similar evaluation methods.

Individual partial EIS Nyquist plots are shown in **Figure 9**, here simulated for three different temperatures (5, 20, 35 °C). The shape and magnitude of the partial impedance spectra are quite diverse. A common feature of all spectra is that they are thermally activated, that is, impedance response increases with decreasing temperature. Another feature of most spectra is that the high-frequency limit extends to the origin of the Nyquist plot, as all plots represent only one individual physicochemical process. The ohmic impedances ( $Z_{cc}$ ,  $Z_{ohm,elyte}^*$ ) are an exception. The current collection system ( $Z_{cc}$ , panel (a)) appears as a single point. Interestingly, the electrolyte ( $Z_{ohm,elyte}^*$ , panel (b)) shows a

considerable complexity with three arcs. The concentration impedance of the electrolyte ( $Z_{conc,elyte}^*$ , panel (c)), in contrast, appears as single semicircle. These three impedances are quite low.

The activation impedance of the graphite anode ( $Z_{act,C_6}^*$ , panel (d)) shows as ideal semicircle, representing the behavior of the charge-transfer resistance coupled to the electrochemical double layer. The composite cathode shows a more complex activation impedance ( $Z_{act,NCA}^*$  and  $Z_{act,LCO}^*$ , panels (e,f)). Both materials show a dominating semicircle due to charge-transfer reaction and double layer, as for the anode. However, this feature is extended at low frequency toward additional capacitive and inductive loops for LCO and NCA, respectively. These loops represent the interparticle lithium transport dynamics which affect individual equilibrium potential and therefore activation impedance.

The concentration impedances of the three AMs show the most complex behavior. The partial EIS of the graphite anode ( $Z_{conc,C_6}^*$ , panel (g)) shows an increase in both real and negative imaginary parts with decreasing frequency. This indicates a distorted Warburg-type behavior, however far off from an ideal Warburg (45° slope in the Nyquist plot) that would be expected from an ideal diffusion process. The spectra furthermore feature a loop, which is pronounced for the 5 °C simulation. The behavior of the cathode materials is even more complex. NCA

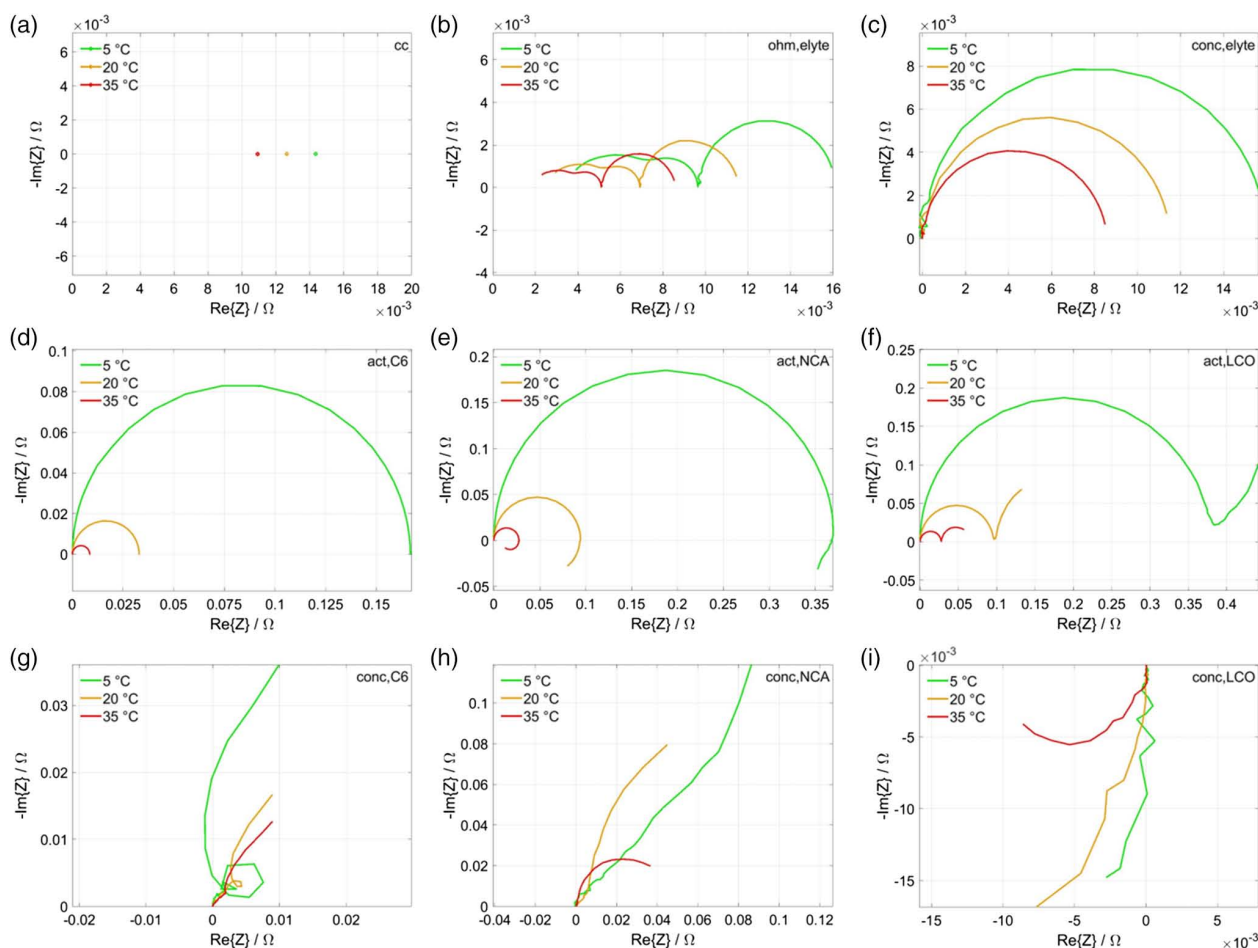


**Figure 9.** Partial electrochemical impedance spectra in Nyquist representation, 50% SOC, and three temperatures (5, 20, 35 °C).

( $Z_{\text{conc,NCA}}^*$ , panel (h)) features a Warburg-type behavior at 5 °C, but a resistor–capacitor (RC) type behavior at the higher temperatures. LCO ( $Z_{\text{conc,LCO}}^*$ , panel (i)) shows large semicircles with positive imaginary part and negative real part. We believe that the uncommon impedance behavior of LCO and NCA is, again, due to interparticle lithium transport processes.

The imaginary parts of the activation and concentration contributions of the individual cathode blend materials are shown in Bode representation in **Figure 10**. While the sum ( $Z_{\text{act+conc}}^*$ ) is identical for NCA and LCO, the individual contributions ( $Z_{\text{act}}^*$  and  $Z_{\text{conc}}^*$ ) strongly differ for low frequencies (<0.1 Hz). In particular, the sign of  $Z_{\text{conc}}^*$  is inverse for the two materials, again indicative of the interparticle lithium transport.

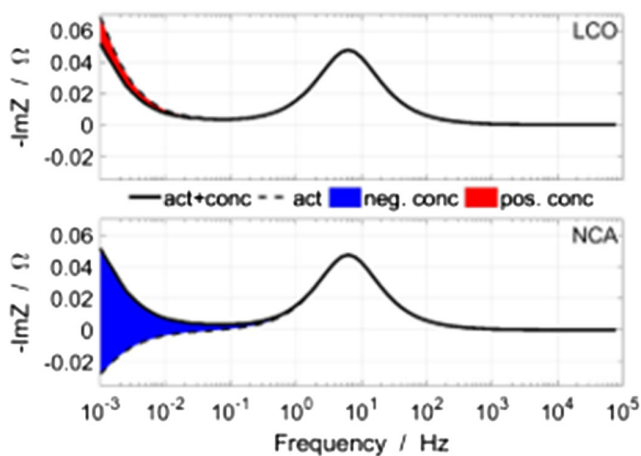


**Figure 10.** Concentration and activation impedance response at 50% SOC and 20 °C for the two AMs in the blend cathode.

### 4.3. Sensitivity Analysis

The macroscopic cell performance is affected by its multiscale design on cell, electrode, and particle level. We have conducted a sensitivity analysis to quantify the influence of various cell parameters on macroscopic observables, specifically the discharge capacity, the internal resistance at 50% SOC, and the impedance at 1 kHz and 50% SOC. These three observables were chosen because they are typically given in battery data sheets. Twenty model parameters representing design variables and material properties on all scales were individually varied and their influence on the observables quantified as described in Section 3.3. Note that a relative sensitivity of unity means direct proportionality between the observable and the parameter.

Results of the analysis are shown in **Figure 11** as bar plot, with one panel for each observable and an individual bar for each parameter. The cell capacity (panel (a)) was determined after a 5 C discharge with CCCV protocol. This protocol was chosen for the analysis because, at the end of the CV phase, the capacity becomes independent of overpotentials (no capacity-rate effect). Therefore, the influence of parameters on capacity can be studied independently from their influence on overpotentials or internal resistance, which will be discussed further later. The cell capacity is trivially dominated by the cell thickness, which increases the active electrode area and therefore the cell capacity proportionally and hence with a sensitivity of unity. Note that here we assume that a change in cell thickness results from a change in the number of electrode pairs inside the cell, not a change in electrode thicknesses. The latter is studied via the individual parameters for the anode and the cathode thicknesses  $d_{\text{an}}$ ,  $d_{\text{ca}}$ . The capacity exhibits sensitivities on these parameters of 0.47 and 0.52, respectively. This means that increasing the thickness of either electrode by 10% would increase the observed cell capacity by

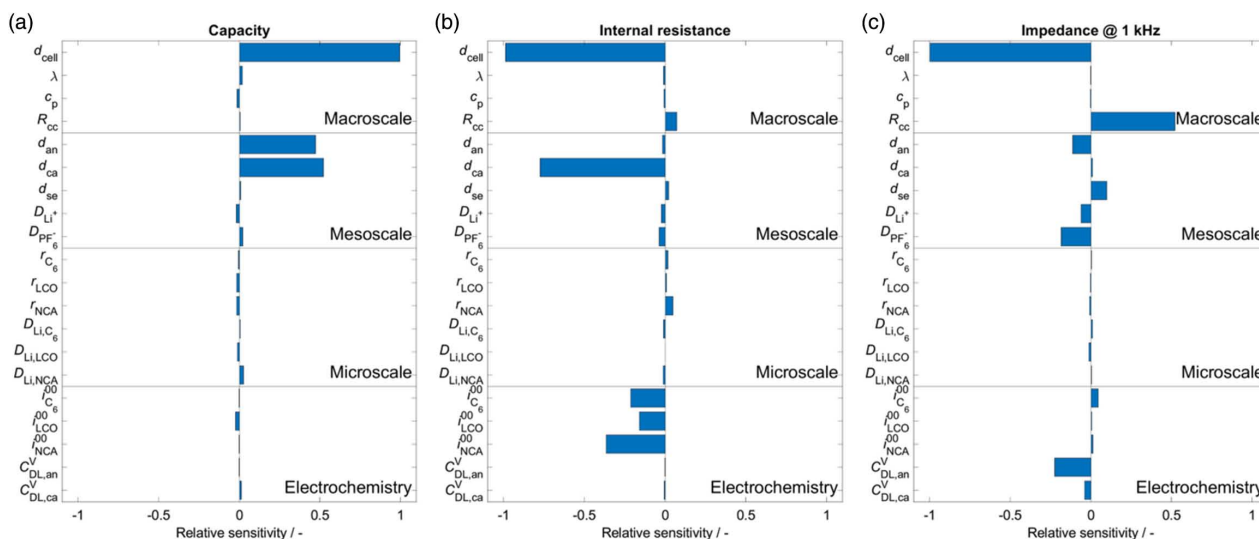


**Figure 11.** Sensitivity of the three characteristic cell-level observables: a) discharge capacity after 5 C CCCV discharge, b) internal resistance at 50% SOC (1 C pulse, 3 s), and c) absolute impedance at 1 kHz (50% SOC), with respect to cell parameters on all scales. All values at 20 °C. The parameters varied are cell thickness ( $d_{\text{cell}}$ ), heat conductivity ( $\lambda$ ), heat capacity ( $c_p$ ), ohmic resistance of current collection system ( $R_{\text{cc}}$ ), anode thickness ( $d_{\text{an}}$ ), cathode thickness ( $d_{\text{ca}}$ ), separator thickness ( $d_{\text{se}}$ ), electrolyte-dissolved species diffusion coefficients ( $D_{\text{Li}^+}$ ,  $D_{\text{PF}_6^-}$ ), radius of AM particles ( $r_{\text{c}_6}$ ,  $r_{\text{LCO}}$ ,  $r_{\text{NCA}}$ ), solid state diffusion coefficient of species in AMs ( $D_{\text{LiC}_6}$ ,  $D_{\text{LiLCO}}$ ,  $D_{\text{LiNCA}}$ ), exchange current density factors ( $i_{\text{c}_6}^0$ ,  $i_{\text{LCO}}^0$ ,  $i_{\text{NCA}}^0$ ), and double-layer capacitances ( $C_{\text{DL,an}}^V$ ,  $C_{\text{DL,ca}}^V$ ).



4.7% and 5.2%, respectively. The results show that the two electrodes are well balanced, else there would be only one single sensitive electrode. All other parameters show sensitivities smaller than  $\pm 0.05$ , some positive and some negative. This confirms that overpotentials do not influence the cell capacity for the performed CCCV discharge protocol.

The influence of cell parameters on the internal resistance is shown in Figure 11b. Again, the sensitivity of minus unity with respect to cell thickness, providing more electrode area inside the cell and therefore decreasing internal resistance, is trivial. The further dominating sensitivity is observed from the cathode thickness,  $d_{ca}$ . It is negative, meaning that an increase in thickness decreases the internal resistance. Other major influences arise from the exchange current densities of the three charge-transfer reactions,  $i_{C_6}^{00}$ ,  $i_{LCO}^{00}$ ,  $i_{NCA}^{00}$ . Small, but notable sensitivities are seen for the ohmic resistance of the current collection system  $R_{cc}$ , as well as AM particle sizes (e.g.,  $r_{NCA}$ ); increasing these parameters increases the internal resistance.

The impedance at 1 kHz shows the most diverse sensitivity on cell parameters, as shown in Figure 11c. The current collection resistance  $R_{cc}$  and the separator thickness  $d_{se}$  show high positive sensitivities, while diffusion coefficients  $D_{Li^+}$ ,  $D_{PF_6^-}$  show negative sensitivities. These are the parameters related to ohmic resistances of electron and ion conductors, and therefore are associated with the high-frequency impedance response. The anode double-layer capacitance  $C_{DL,an}^V$  shows also a considerable sensitivity, related to the fact that the frequency of 1 kHz is well within the anode response (cf., Figure 8).

It is interesting to investigate the sensitivity of the cell parameters on the individual overpotential contributions. These results are shown in Figure 12 for a 5 C discharge (averaged between 40% and 60% SOC). The current collection resistance ( $R_{cc}$ ) shows a sensitivity of unity toward the current collection overpotential ( $\eta_{cc}$ , panel (a)), as required from its definition (Equation (6)). All other overpotentials show a more complex dependency, being sensitive on several parameters. The ohmic and concentration resistances of the electrolyte ( $\eta_{ohm,elyte}$ ,  $\eta_{conc,elyte}$ , panels (b,c)) depend on all layer thicknesses ( $d_{an}$ ,  $d_{ca}$ ,  $d_{se}$ ) and the  $Li^+$  diffusion coefficient ( $D_{Li^+}$ ). The activation overpotentials ( $\eta_{act,C_6}$ ,  $\eta_{act,LCO}$ ,  $\eta_{act,NCA}$ , panels (d–f)) depend not only on their respective exchange current densities  $i^{00}$ , as expected, but also on the respective electrode thicknesses as well as on other parameters. The graphite concentration overpotential ( $\eta_{conc,C_6}$ , panel (g)) shows sensitivities not only on the microscale parameters  $D_{C_6}$  and  $r_{C_6}$ , as would be physically expected, but also on additional macroscale parameters, including the cathode thickness  $d_{ca}$ . A further analysis of this counterintuitive result revealed that this is due to the debalancing of the electrodes when only cathode thickness is changed:  $\eta_{conc,C_6}$  depends on SOC (cf., Figure 6), but the electrode-individual SOC is different in the debalanced cell, leading to a different overpotential at the same nominal SOC. A similar interpretation applies to the sensitivity of  $\eta_{conc,C_6}$  on the anode thickness. The behavior is even more complex for the concentration overpotentials of the cathode materials ( $\eta_{conc,LCO}$ ,  $\eta_{conc,NCA}$ , panels (h,i)) that show cross-sensitivities with each other's related physical parameters.

Overall, the sensitivity analyses demonstrate the strong and nonlinear influences of design and material parameters on

macroscopic cell properties and overpotential contributions. Some sensitivities are immediately obvious, others can be easily interpreted, but some are unexpected or even seem counterintuitive. There is no single design or material parameter affecting cell properties such as capacity or internal resistance. Instead, macroscopic properties are influenced by a multitude of parameters. This explains the difficulty of optimizing the cell performance in practice, but at the same time gives valuable insight and provides direction for doing so.

## 5. Summary and Conclusions

In this article, we have developed and applied three methodologies for model-based interpretation and visualization of lithium-ion battery performance: 1) deconvolution of overpotential contributions, 2) partial electrochemical impedance spectroscopy, and 3) sensitivity analyses. The methods were applied to a previously developed and validated model of a commercial high-power lithium-ion pouch cell. The main findings can be summarized as follows: 1) physicochemical model expressions and simulation methodology were developed for quantifying different contributions to the total cell overpotential: ohmic overpotentials of current collection system and electrolyte; concentration overpotential of the electrolyte; activation overpotentials of all AMs; and concentration overpotentials of all AMs. The contributions show a nonlinear variation with operation parameters such as C-rate and ambient temperature. Concentration overpotentials in the graphite AM dominate the behavior at high currents. 2) We have introduced the concept of partial electrochemical impedance spectroscopy, allowing to simulate the frequency-domain response of the quantified overpotential contributions. This enables the direct visualization of the origin of various impedance features. The individual processes show diverse spectra in the Nyquist representation. Different to the time-domain results, the dominating impedance contribution arises from the cathode. We conclude that impedance spectroscopy at open circuit cannot necessarily be used to draw conclusions on the cell performance under high currents. 3) Systematic sensitivity analyses were conducted, which allowed to quantify the influence of cell design and material parameters on macroscopic observables such as capacity, internal resistance, and impedance. The analysis revealed diverse and nonlinear sensitivities. No single parameter dominates the cell performance, showing that the studied cell is well designed. 4) The investigated cell features a blend cathode. This complicates both the methodology and the interpretation of the results. The two blend components show strong coupling, leading to particular features in the partial impedance spectra and cross-sensitivities.

The combined results enable a detailed insight into the performance properties and limitations of the studied lithium-ion pouch cell. They provide guidelines toward further cell optimization, using an understanding-based approach. The methodologies are not restricted to the present cell, but can be applied to arbitrary models of real or virtual cells. They are therefore a useful toolbox within future modeling and simulation studies.

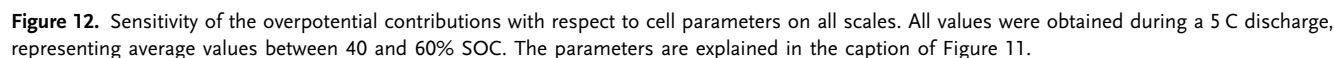


**Table A1.** Symbol list.

Symbol	Unit	Meaning
$c_i$	$\text{mol} \cdot \text{m}^{-3}$	Concentration of species $i$
$C_N$	A·s	Nominal capacity
$c_p$	$\text{J} \cdot \text{kg}^{-1} \cdot \text{K}^{-1}$	Heat capacity
$C_{\text{DL}}^V$	$\text{F} \cdot \text{m}^{-3}$	Volume-specific double-layer capacity
$d$	m	Thickness (cell, anode, cathode, separator)
$D_i$	$\text{m}^2 \cdot \text{s}^{-1}$	Diffusion coefficient of species $i$
$f_{ji}$	–	Relative sensitivity
$f_\eta$	–	Correction factor for the overpotential contribution
$F$	$\text{C} \cdot \text{mol}^{-1}$	Faraday's constant
$i$	$\text{A} \cdot \text{m}^{-2}$	Area-specific current
$i^0$	$\text{A} \cdot \text{m}^{-2}$	Exchange current density factor
$I$	A	Current
$n_{\text{Li}}$	mol	Amount of lithium within the active material
$O_j$	–	Observable during sensitivity analysis
$P_i$	–	Model parameter
$r$	m	Radius of active material particle
$R$	$\text{J} \cdot \text{K}^{-1} \cdot \text{mol}^{-1}$	Ideal gas constant
$R_{\text{cc}}$	$\Omega \cdot \text{m}^2$	Area-specific ohmic resistance of current collection system
$R_i$	$\Omega$	Internal resistance
$T$	K	Temperature
$V$	V	Operating voltage
$V^{\text{eq}}$	V	Equilibrium voltage
$X_{\text{Li}}$	1	Stoichiometry of lithium within the active material
$Z^*$	$\Omega$	Complex frequency-domain impedance
$\Delta\phi$	V	Electric potential difference between electrode and electrolyte
$\Delta\phi^{\text{eq}}$	V	Equilibrium potential difference
$\eta$	V	Overpotential
$\lambda$	$\text{W} \cdot \text{m}^{-1} \cdot \text{K}^{-1}$	Heat conductivity
$\phi_{\text{elyte}}$	V	Electric potential of the electrolyte

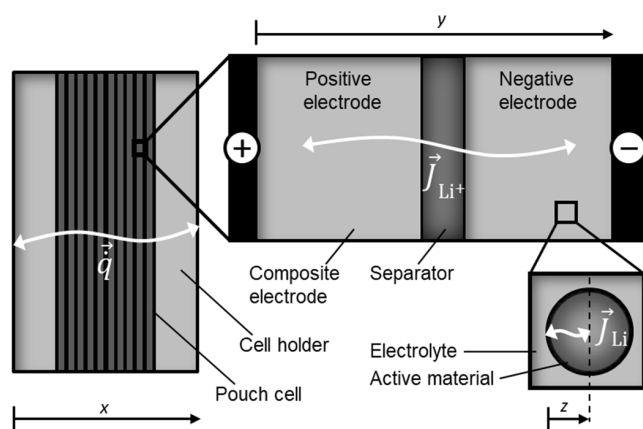


**Figure A1.** 1D + 1D + 1D (pseudo-3D or P3D) modeling domain.

## 6. Appendix

### 6.1. Symbol List

A list of symbols used in the main body of the article is shown in Table A1.

**Table A2.** Model equations.  $A_e$ — $\text{m}^2$ —active electrode area;  $A_n^V$ — $\text{m}^2 \cdot \text{m}^{-3}$ —volume-specific surface area of reaction  $n$ ;  $C_{\text{DL}}^V$ — $\text{F} \cdot \text{m}^{-3}$ —volume-specific double-layer capacity;  $c_i$ — $\text{mol} \cdot \text{m}^{-3}$ —concentration of species  $i$  in a bulk phase;  $c_{\text{Li}}$ — $\text{mol} \cdot \text{m}^{-3}$ —concentration of lithium in the active material;  $c_{p,i}^0$ — $\text{J} \cdot \text{mol}^{-1} \cdot \text{K}^{-1}$ —molar heat capacity of species  $i$ ;  $c_p$ — $\text{J} \cdot \text{kg}^{-1} \cdot \text{K}^{-1}$ —specific heat capacity;  $D_i$ — $\text{m}^2 \cdot \text{s}^{-1}$ —diffusion coefficient of species  $i$ ;  $D_i^{\text{eff}}$ — $\text{m}^2 \cdot \text{s}^{-1}$ —effective diffusion coefficient of species  $i$ ;  $E_a$ — $\text{J} \cdot \text{mol}^{-1}$ —activation energy;  $F$ — $\text{C} \cdot \text{mol}^{-1}$ —Faraday's constant;  $\Delta H_n$ — $\text{J} \cdot \text{mol}^{-1}$ —reaction enthalpy of reaction  $n$ ;  $i$ — $\text{A} \cdot \text{m}^{-2}$ —area-specific current (with respect to  $A_e$ );  $i^0$ — $\text{A} \cdot \text{m}^{-2}$ —exchange current density;  $i_{\text{DL}}^V$ — $\text{A} \cdot \text{m}^{-3}$ —volume-specific current due to double layer;  $i_f^V$ — $\text{A} \cdot \text{m}^{-3}$ —volume-specific faradaic current;  $I_{\text{cell}}$ —A—current of the cell;  $j$ — $\text{m}^2 \cdot \text{s}^{-1}$ —index of bulk phases;  $J_q$ — $\text{W} \cdot \text{m}^{-2}$ —heat flux from cell surface;  $J_i$ — $\text{mol} \cdot \text{m}^{-2} \cdot \text{s}^{-1}$ —molar flux of species  $i$ ;  $L_{\text{ep}}$ —m—thickness of electrode pair;  $M_i$ — $\text{kg} \cdot \text{mol}^{-1}$ —molar mass of species  $i$ ;  $n$ — $\text{mol} \cdot \text{m}^{-3}$ —index for reactions;  $N_p$ —1—number of products participating in reaction;  $N_R$ —1—number of reactants participating in reaction;  $N_r$ —1—number of reactions;  $\dot{q}_{\text{chem}}$ — $\text{W} \cdot \text{m}^{-2}$ —heat source due to chemical reactions;  $\dot{q}_{\text{ohm}}$ — $\text{W} \cdot \text{m}^{-2}$ —heat source due to ohmic losses;  $\dot{q}^V$ — $\text{W} \cdot \text{m}^{-3}$ —volume-specific heat source;  $R$ — $\text{J} \cdot \text{K}^{-1} \cdot \text{mol}^{-1}$ —ideal gas constant;  $R_{\text{cc}}$ — $\Omega \cdot \text{m}^2$ —area-specific ohmic resistance of current collection system;  $R_{\text{SEI}}^V$ — $\Omega \cdot \text{m}^3$ —volume-specific ohmic resistance of SEI film;  $r_n$ — $\text{mol} \cdot \text{m}^{-2} \cdot \text{s}^{-1}$ —interfacial reaction rate of reaction  $n$ ;  $s_i^V$ — $\text{mol} \cdot \text{m}^{-3} \cdot \text{s}^{-1}$ —volumetric species source term;  $s_{i,\text{DL}}^V$ — $\text{mol} \cdot \text{m}^{-3} \cdot \text{s}^{-1}$ —volumetric species source term due to double-layer charge/discharge;  $t$ —s—time;  $T$ —K—temperature;  $T_{\text{amb}}$ —K—ambient temperature (cell surrounding);  $V$ —V—cell voltage;  $V_{\text{cell}}$ — $\text{m}^3$ —volume of cell;  $x$ —m—spatial position in dimension of battery thickness;  $y$ —m—spatial position in dimension of electrode-pair thickness;  $z$ —m—spatial position in dimension of particle thickness;  $z$ —1—number of electrons transferred in charge-transfer reaction;  $\alpha$ — $\text{W} \cdot \text{m}^{-2} \cdot \text{K}^{-1}$ —heat transfer coefficient;  $\beta_n$ —1—transfer coefficients of electrochemical reaction  $n$ ;  $\phi_{\text{elyt}}$ —V—electric potential in the electrolyte;  $\phi_{\text{elde,an}}$ —V—electric potential of the anode electrode;  $\phi_{\text{elde,ca}}$ —V—electric potential of the cathode electrode;  $\Delta\phi^{\text{eff}}$ —V—effective electric potential difference;  $\Delta\phi^{\text{eq}}$ —V—equilibrium potential difference;  $\Delta\phi$ —V—electric potential difference between electrode and electrolyte;  $\epsilon$ —1—emissivity of the cell surface;  $\epsilon_{\text{elyt}}$ —1—volume fraction of the electrolyte;  $\epsilon_j$ —1—volume fraction of bulk phase  $j$ ;  $\eta_{\text{act}}$ —V—activation overpotential;  $\lambda$ — $\text{W} \cdot \text{m}^{-1} \cdot \text{K}^{-1}$ —thermal conductivity;  $\nu_i$ —1—stoichiometric coefficient of species  $i$ ;  $\nu_e$ —1—stoichiometric coefficient of electron;  $\rho$ — $\text{kg} \cdot \text{m}^{-3}$ —density;  $\sigma$ — $\text{S} \cdot \text{m}^{-1}$ —electrolyte conductivity;  $\sigma_{\text{SB}}$ — $\text{W} \cdot \text{m}^{-2} \cdot \text{K}^{-4}$ —Stefan-Boltzmann constant;  $\tau_{\text{elyt}}$ —1—geometric tortuosity of the electrolyte.

#### Macroscale ( $x$ direction): heat transport in cell

$$\begin{aligned} \text{Energy conservation} & \quad \rho c_p \frac{\partial T}{\partial t} = \frac{\partial}{\partial x} \left( \lambda \frac{\partial T}{\partial x} \right) + \dot{q}^V \\ \text{Heat flux at cell surface} & \quad J_q = \alpha (T - T_{\text{amb}}) + \epsilon \sigma_{\text{SB}} (T^4 - T_{\text{amb}}^4) \\ \text{Total heat sources} & \quad \dot{q}^V = \frac{A_{\text{cell}}}{V_{\text{cell}}} \left( \int_0^{L_{\text{ep}}} (\dot{q}_{\text{chem}}(y) + \dot{q}_{\text{ohm}}(y)) dy + R_{\text{cc}} i^2 \right) \\ \text{Chemistry heat source} & \quad \dot{q}_{\text{chem}} = \sum_{n=1}^{N_r} (r_n A_n^V (-\Delta H_n + F \nu_{e,n} \Delta\phi_n)) \\ \text{Ohmic heating} & \quad \dot{q}_{\text{ohm}} = \sigma_{\text{elyt}} \cdot \left( \frac{\partial \phi_{\text{elyt}}}{\partial y} \right)^2 \end{aligned}$$

#### Mesoscale ( $y$ direction): mass and charge transport in electrode pair

$$\begin{aligned} \text{Mass conservation of species } i & \quad \frac{\partial (c_{\text{elyt}} c_i)}{\partial t} = - \frac{\partial j_i}{\partial y} + s_i^V + s_{i,\text{DL}}^V \end{aligned}$$

**Table A2.** Continued.

<b>Macroscale (x direction): heat transport in cell</b>	
Charge conservation	$C_{DL}^V \frac{\partial(\Delta\phi)}{\partial t} = \sum_i z_i F \frac{\partial j_i}{\partial y} - i_F^V$
Species fluxes: Nernst–Planck	$J_i = -D_i^{\text{eff}} \frac{\partial c_i}{\partial y} - \frac{z_i F}{RT} c_i D_i^{\text{eff}} \frac{\partial \phi_{\text{act},n}}{\partial y}$
<b>Microscale (z direction): mass transport in active materials particle</b>	
Mass conservation (Fick's second law)	$\frac{\partial c_{Li,AM}}{\partial t} = \frac{1}{z^2} \frac{\partial}{\partial z} \left( z^2 D_{Li,AM} \frac{\partial c_{Li,AM}}{\partial z} \right)$
<b>Electrochemistry<sup>a)</sup></b>	
Interfacial rate of reaction $n$	$r_n = \frac{j_n}{F} = \frac{j_n^0}{F} \left[ \exp \left( \frac{\beta_n z F}{RT} \eta_{\text{act},n} \right) - \exp \left( -\frac{(1-\beta_n) z F}{RT} \eta_{\text{act},n} \right) \right]$
Exchange current density	$j_n^0 = j_n^{00} \cdot \exp \left( -\frac{E_{\text{ex},n}}{RT} \right) \cdot \prod_{i=1}^{N_R} \left( \frac{c_i}{c_i^0} \right)^{(1-\beta_n) \nu_i} \prod_{i=1}^{N_P} \left( \frac{c_i}{c_i^0} \right)^{\beta_n \nu_i'}$
Activation overpotential	$\eta_{\text{act},n} = \Delta\phi^{\text{eff}} - \Delta\phi^{\text{eq}} = \Delta\phi - R_{\text{SEI}}^V \frac{i_F^V}{i_F^V} - \Delta\phi_n^{\text{eq}}$
Species source terms	$s_i^V = \sum_{n=1}^{N_i} (\nu_i r_n A_n^V)$
<b>Current, voltage, potentials</b>	
Cell voltage	$V = \phi_{\text{elde,ca}} - \phi_{\text{elde,an}} - i \cdot R_{\text{cc}}$
Cell current	$I_{\text{cell}} = \frac{A_{\text{cell}}}{V_{\text{cell}}} \cdot \int_{y=0}^{L_{\text{electrode}}} (i_F^V + i_{DL}^V) dy$
Faradaic current density	$i_F^V = F s_e^V = \sum_{n=1}^{N_e} F (\nu_{e,n} r_n A_n^V)$
Double-layer current density	$i_{DL}^V = C_{DL}^V \frac{d(\Delta\phi)}{dt}$
Source term from double layer	$s_{i,DL}^V = \frac{z_i}{F} i_{DL}^V$ with $i = \text{Li}^+$
Potential step (anode and cathode)	$\Delta\phi = \phi_{\text{elde}} - \phi_{\text{elyt}}$
<b>Multiphase management</b>	
Volume fraction of phases	$\frac{\partial(\rho_i c_i)}{\partial t} = \sum_{j=1}^{N_{R,j}, N_{P,j}} s_j^V M_i$
Feedback on transport coefficients (porous electrode theory)	$D_i^{\text{eff}} = \frac{\epsilon_{\text{elyt}}}{\tau_{\text{elyt}}} D_i$

<sup>a)</sup>As implemented in Cantera.<sup>[28,29]</sup>

## 6.2. Model Description

The physicochemical model used here as basis for the investigations was developed and parameterized by Carelli et al. and Kupper et al.<sup>[13,27]</sup> The pseudo-3D modeling domain is shown in **Figure A1**. All model equations, including a definition of the symbols, are shown in **Table A2**.

## Acknowledgements

This work was funded by the German Research Foundation (DFG) in the framework of the research training group SiMET – Simulation of Mechanical, Electrical and Thermal Effects in Lithium-ion Batteries (281041241/GRK 2218).

Open access funding enabled and organized by Projekt DEAL.

## Conflict of Interest

The authors declare no conflict of interest.

## Data Availability Statement

Research data are not shared.

## Keywords

blend electrodes, lithium-ion batteries, overpotentials, partial electrochemical impedance spectroscopy, sensitivity analyses

Received: December 22, 2020

Revised: February 15, 2021

Published online: April 9, 2021

- [1] C. Julien, A. Mauger, A. Vijn, K. Zaghib (Eds.) *Lithium Batteries*, Springer, Cham, Switzerland **2016**.
- [2] S. G. Chalk, J. F. Miller, *J. Power Sources* **2006**, 159, 73.
- [3] A. Opitz, P. Badami, L. Shen, K. Vignarooban, A. M. Kannan, *Renew. Sustain. Energy Rev.* **2017**, 68, 685.
- [4] Y. Merla, B. Wu, V. Yufit, R. F. Martinez-Botas, G. J. Offer, *J. Power Sources* **2018**, 384, 66.
- [5] S. De, P. W.C. Northrop, V. Ramadesigan, V. R. Subramanian, *J. Power Sources* **2013**, 227, 161.
- [6] D. Gröbl, W. G. Bessler, *J. Power Sources* **2015**, 297, 481.
- [7] U. Krewer, F. Röder, E. Harinath, R. D. Braatz, B. Bedürftig, R. Findeisen, *J. Electrochem. Soc.* **2018**, 165, A3656.
- [8] S. C. DeCaluwe, P. J. Weddle, H. Zhu, A. M. Colclasure, W. G. Bessler, G. S. Jackson, R. J. Kee, *J. Electrochem. Soc.* **2018**, 165, E637.
- [9] S. Barcellona, L. Piegari, *Energies* **2017**, 10, 2007.
- [10] D. Grazioli, M. Magri, A. Salvadori, *Comput. Mech.* **2016**, 58, 889.
- [11] D. Miranda, C. M. Costa, S. Lancers-Mendez, *J. Electroanal. Chem.* **2015**, 739, 97.
- [12] A. A. Franco, *RSC Adv.* **2013**, 3, 13027.
- [13] S. Carelli, M. Quarti, M. C. Yagci, W. G. Bessler, *J. Electrochem. Soc.* **2019**, 166, A2990.
- [14] P. W. Atkins, J. D. Paula, *Atkins' Physical Chemistry*, Oxford University Press, Oxford, Great Britain, **2006**, p. 938.
- [15] J. Newman, K. E. Thomas-Alyea, *Electrochemical Systems*, John Wiley & Sons, Hoboken, NJ, **2004**.
- [16] B. Weißhar, W. G. Bessler, *J. Energy Storage* **2017**, 14, 179.
- [17] C. Kupper, B. Weißhar, S. Reißmann, W. G. Bessler, *J. Electrochem. Soc.* **2018**, 165, A3468.
- [18] E. Barsoukov, J. R. MacDonald (Eds.) *Impedance Spectroscopy. Theory, Experiment, and Applications*, John Wiley & Sons, Hoboken, NJ, **2005**.
- [19] M. Doyle, J. P. Meyers, J. Newman, *J. Electrochem. Soc.* **2000**, 147, 99.
- [20] W. G. Bessler, *Solid State Ionics* **2005**, 176, 997.
- [21] S. Gewies, W. G. Bessler, *J. Electrochem. Soc.* **2008**, 155, B937.
- [22] M. A. Kramer, H. Rabitz, J. M. Calo, R. J. Kee, *Int. J. Chem. Kinet.* **1984**, 16, 559.
- [23] P. Glarborg, J. A. Miller, R. J. Kee, *Combust. Flame* **1986**, 65, 177.
- [24] J. E. Dove, J. Warnatz, *Berichte der Bunsengesellschaft für physikalische Chemie* **1983**, 87, 1040.
- [25] F. Behrendt, O. Deutschmann, U. Maas, J. Warnatz, *J. Vac. Sci. Technol. A: Vac. Surf. Films* **1995**, 13, 1373.
- [26] M. Vogler, A. Bieberle-Hütter, L. J. Gauckler, J. Warnatz, W. G. Bessler, *J. Electrochem. Soc.* **2009**, 156, B663.
- [27] C. Kupper, W. G. Bessler, *J. Electrochem. Soc.* **2017**, 164, A304.
- [28] D. G. Goodwin, R. L. Speth, H. K. Moffat, B. W. Weber, Cantera: An Object-Oriented Software Toolkit for Chemical Kinetics, Thermodynamics, and Transport Processes. Zenodo **2021**.
- [29] M. Mayur, S. C. DeCaluwe, B. L. Kee, W. G. Bessler, *Electrochim. Acta* **2019**, 323, 134797.
- [30] W. G. Bessler, S. Gewies, M. Vogler, *Electrochim. Acta* **2007**, 53, 1782.
- [31] F. Hall, J. Touzri, S. Wußler, H. Buqa, W. G. Bessler, *J. Energy Storage* **2018**, 17, 109.



- [32] W. G. Bessler, *J. Electrochem. Soc.* **2007**, 154, B1186.  
[33] S. Gantenbein, M. Weiss, E. Ivers-Tiffée, *J. Power Sources* **2018**, 379, 317.  
[34] A. Jossen, *J. Power Sources* **2006**, 154, 530.  
[35] D. Andre, M. Meiler, K. Steiner, C. Wimmer, T. Soczka-Guth, D. U. Sauer, *J. Power Sources* **2011**, 196, 5334.